

# Supporting Information

## Protein Induces Layer-by-Layer Exfoliation of Transition Metal Dichalcogenides

Guijian Guan,<sup>†,‡</sup> Shuangyuan Zhang,<sup>‡</sup> Shuhua Liu,<sup>‡</sup> Yongqing Cai,<sup>†</sup> Michelle Low,<sup>‡</sup> Choon Peng Teng,<sup>‡</sup> In Yee Phang,<sup>‡</sup> Yuan Cheng,<sup>†</sup> Koh Leng Duei,<sup>‡</sup> Bharathi Madurai Srinivasan,<sup>†</sup> Yuangang Zheng,<sup>‡</sup> Yong-Wei Zhang,<sup>\*,†</sup> and Ming-Yong Han<sup>\*,‡</sup>

<sup>†</sup>Institute of High Performance Computing, A\*STAR, 1 Fusionopolis Way, Singapore 138632

<sup>‡</sup>Institute of Materials Research and Engineering, A\*STAR, 3 Research Link, Singapore 117602

\*E-mails: zhangyw@ihpc.a-star.edu.sg; my-han@imre.a-star.edu.sg

### I. Materials and Methods

**Materials.** Molybdenum sulfide (MoS<sub>2</sub>), tungsten disulfide (WS<sub>2</sub>), graphite flake, glutathione, methacrylic acid, glycine, citric acid, benzoic acid, phenylacetic acid, aniline, phenethylamine, phenylalanine, bovine serum albumin (BSA), polyacrylic acid (PAA), polyvinylpyrrolidone (PVP), chitosan, gelatin, 3-(4,5-dimethylthiazol-2-yl)-2,5-diphenyltetrazolium bromide (MTT), 2,4-dichlorophenoxyacetic acid (2,4-DA), sodium sulfate (Na<sub>2</sub>SO<sub>4</sub>), hydrochloric acid, sodium hydroxide, dimethyl sulphoxide (DMSO) and Nafion were purchased from Sigma-Aldrich. Phosphate buffer powder (pH=7.4) and methanol were obtained from Honeywell. All chemicals were used without further purification, and their aqueous solutions were prepared using distilled water.

**BSA-induced exfoliation of layered materials in water.** The exfoliation of layered materials was achieved by using a sonic bath with a low energy density, Elma Elmasonic E100H. Typically, 50 mg of MoS<sub>2</sub> powder was added into 10 mL of aqueous solution containing 10 mg of BSA. The mixed suspension was sonicated for 48 h. After centrifuged at 5000 rpm for 45 min, the collected precipitant was re-dispersed into water via sonication for 10 min. The resulting solution was further centrifuged at 1500 rpm for 45 min, and the supernatant was obtained containing MoS<sub>2</sub>-BSA nanosheets in water. Alternatively, various small molecules (glutathione, methacrylic acid, glycine, citric acid, benzoic acid, phenylacetic acid, aniline, phenethylamine and phenylalanine) and

polymers (PAA, PVP, chitosan and gelatin) were used to replace BSA for preparing MoS<sub>2</sub> nanosheets under the identical procedure. Similarly, 50 mg of WS<sub>2</sub> powder and graphite were also separately sonicated in 10 mL of aqueous solution containing 10 and 5 mg of BSA for 48 h, respectively. The remaining procedure was kept the same as described above to obtain WS<sub>2</sub> nanosheets and graphene. To understand the mechanism for exfoliating MoS<sub>2</sub> nanosheets, 50 mg of MoS<sub>2</sub> powder was separately added into 10 mL of aqueous solution containing different amount of BSA (0, 1, 2, 5, 10, 20, 30, 40, 50, 100 and 150 mg) followed by sonication for 48 h. Also, different amount of MoS<sub>2</sub> powder (10, 20, 50, 80, 100, 200, 300, 500 and 1000 mg) was separately added into 10 mL of aqueous solution containing 10 mg of BSA followed by sonication for 48 h.

**Binding energy simulation of different functional groups on various nanosheets.** First-principles calculations based on density functional theory (DFT) were performed to evaluate the physical adsorption of various synthetic, bio-polymers and proteins on MoS<sub>2</sub> nanosheets. To uncover their role in the adsorption on MoS<sub>2</sub> nanosheets, we calculated the binding energies of different functional groups/segments of polymers (i.e., basic building blocks) on MoS<sub>2</sub> layer. For this, various molecules including CH<sub>3</sub>-X (X= -OH, -SH, -NH<sub>2</sub>, -COOH, -SSCH<sub>3</sub> and -C<sub>6</sub>H<sub>5</sub>) and CH<sub>3</sub>-CONH-CH<sub>3</sub> were chosen for the simulation by the non-local van der Waals optB88 functional, as implemented in the Vienna Ab initio Simulation Package (VASP) suite. The MoS<sub>2</sub> layer was modeled using 5×5 supercells. The first Brillouin zone was sampled with a 3×3×1 Monkhorst-Pack grid and the energy cutoff of planewave was set to 400 eV. All the structures were relaxed until the force exerted on each atom was less than 0.005 eV/Å. The binding energy ( $E_b$ ) of the given molecules on MoS<sub>2</sub> layer is calculated as  $E_b = E_{\text{MoS}_2\text{-molecule}} - E_{\text{MoS}_2} - E_{\text{molecule}}$ , where  $E_{\text{molecule}}$ ,  $E_{\text{MoS}_2}$ , and  $E_{\text{MoS}_2\text{-molecule}}$  are the energies of the bound molecule, the MoS<sub>2</sub> layer, and the complex of MoS<sub>2</sub> and molecule, respectively. Also, the binding energies of functional groups at the edges of MoS<sub>2</sub> layer were simulated by the optB88 functional, as implemented in the Vienna Ab initio Simulation Package (VASP) suite. The edge of MoS<sub>2</sub> is modeled by constructing a MoS<sub>2</sub> armchair sheet including 12 Mo-S dimer lines across its width. The distance between two nanosheets is set as 17 Å to avoid the spurious interaction of the edge states between the two adjacent edges. Furthermore, the binding energies on WS<sub>2</sub> layer, WSe<sub>2</sub> layer and graphene were calculated as well.

**Biocompatibility test of MoS<sub>2</sub> nanosheets.** Fibroblast cells were seeded at  $2.0 \times 10^4$  cells/cm<sup>2</sup> in 96-well plates and cultured into monolayer. After incubating for 24 h in culture medium containing 10 µg/mL polymer-adsorbed MoS<sub>2</sub> materials in triplicates at 37 °C in a humidified atmosphere containing 5% CO<sub>2</sub>, the cells were first washed with PBS buffer, and 100 µL of 0.1 mg/mL of MTT

assay was then added to each well in the plates. After incubating for 2 h, the solution was removed and 100  $\mu$ L of DMSO was added to release the purple formazan crystals from viable cells. The optical density of the purple formazan crystals was determined at 570 nm with a reference at 630 nm by using an absorbance microplate reader. The viability is calculated by the optical density of the samples divided by that of control cells without treating with various polymer-adsorbed MoS<sub>2</sub> nanosheets.

**Adsorption of 2,4-DA on MoS<sub>2</sub> nanosheets.** Experimentally, 5 mg of polymer-adsorbed MoS<sub>2</sub> nanosheets were dispersed into 5 mL of a mixing solution of methanol/water (4:1) containing different concentration of 2,4-DA. After incubating in a rocking table with shaking at 300 rpm for 12 h, the MoS<sub>2</sub> nanosheets were removed from the solution by centrifugation at 10000 rpm for 10 min. The bound amount of 2,4-DA was determined by measuring the difference between the total amount added and the residual amount in the supernatant by using a UV-vis absorption spectrophotometer at 229 nm.

**Electrochemical measurement of MoS<sub>2</sub> nanosheets.** Electrochemical properties of various polymer-adsorbed MoS<sub>2</sub> nanosheets were examined by using AUTOLAB PGSTAT302N electrochemical workstation in 0.1 M Na<sub>2</sub>SO<sub>4</sub> solution as an electrolyte. Electrochemical analysis was carried out in three-electrode configuration with MoS<sub>2</sub>-modified glass carbon electrode as working electrode, platinum as counter electrode, and Ag/AgCl as reference electrodes. The working electrode was prepared by dropping 20  $\mu$ L of the MoS<sub>2</sub> solution (0.1 mg) for two times, followed by dropping 20  $\mu$ L of Nafion solution (0.5 wt%). After dried at 45 °C for 2 h, the working electrode was placed into electrolyte for measuring electrochemical property. Cyclic voltammetry curves were measured between -0.2 and 0.5 V at different scan rates.

**Characterization.** UV-vis absorption and fluorescence spectra were recorded on a Shimadzu UV-3150 spectrophotometer and a Shimadzu PF-5301PC spectrofluorophotometer, respectively. X-ray diffraction (XRD) of MoS<sub>2</sub> nanosheets were characterized by an X-ray diffractometer (Bruker D8 GADDS) with Cu K $\alpha$  ( $\lambda=0.15406$  nm). Thermogravimetric analysis (TGA) was carried out on a TGA Q5000 under the condition of 10 °C/min with a nitrogen flow at 75 mL/min. Atomic force microscopy (AFM) images were taken by using an AFM Nano First-3100. Transmission electron microscopy (TEM) images were collected on a Philips 300 FEGTEM with the accelerating voltage of 300 kV. Optical photographs were taken under room light with a Canon 350D digital camera. Raman measurements were conducted with Thermo Fisher DXR Raman Microscope equipped with a CCD detector in backscattered configuration using a 10 $\times$  objective, and the Raman spectra were recorded with a 488 nm laser.

## II. Supporting Figures and Discussions

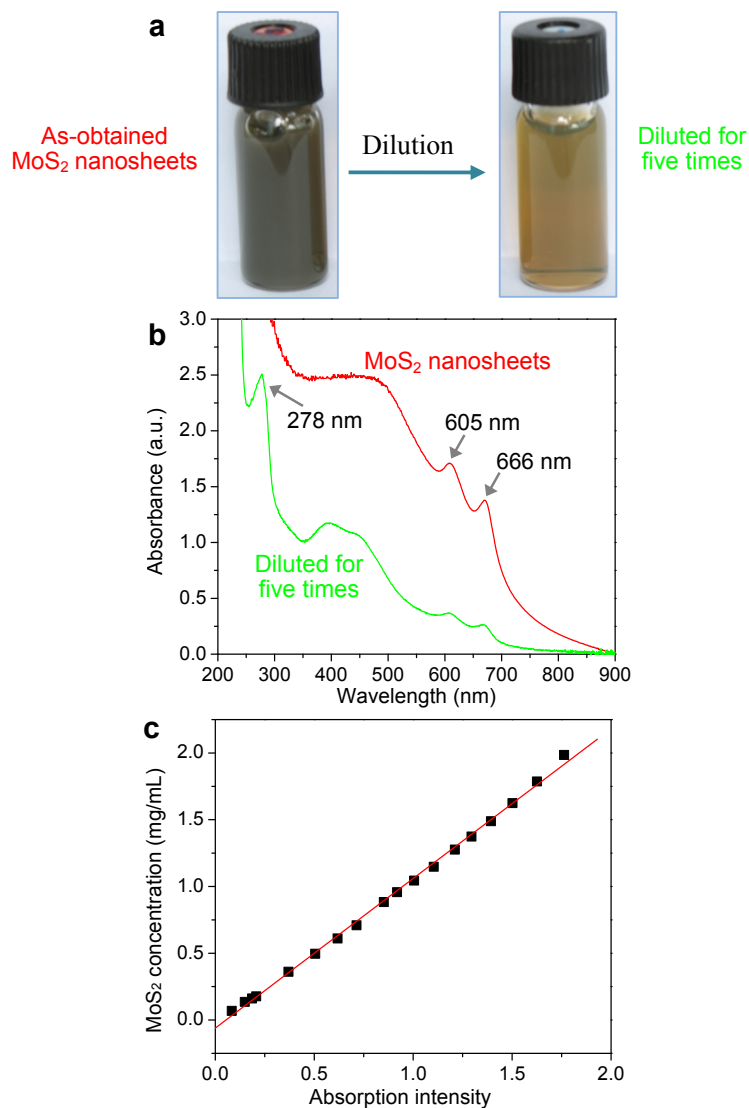


**Figure S1.** Characterization of MoS<sub>2</sub> nanosheets by the optical photographs (a) and UV-vis absorption spectra (b). MoS<sub>2</sub> nanosheets were exfoliated via sonicating a mixture of 50 mg MoS<sub>2</sub> powder and 10 mg BSA in 10 mL of H<sub>2</sub>O by using a sonic bath. After sonication for 48 h, the resultant solution was first centrifuged at 5000 rpm for 45 min to remove free BSA, and the precipitant was re-dispersed into H<sub>2</sub>O by sonication for 10 min. Then, the obtained solution was centrifuged at 1500 rpm for 45 min to remove the non-exfoliated MoS<sub>2</sub>, and the supernatant in dark color (left in A) was extracted to obtain single-layer MoS<sub>2</sub> nanosheets in aqueous solution at pH 6. After dilution for five times (right in A), the absorption peak of BSA (278 nm) in the obtained light yellow solution was observed. (c) Linear relationship of the concentration and absorption intensity at 666 nm of exfoliated MoS<sub>2</sub> nanosheets in H<sub>2</sub>O, which can be used to estimate the amount of exfoliated MoS<sub>2</sub> nanosheets by the comparison of absorption intensity. Different concentration of MoS<sub>2</sub> nanosheets were obtained via the dilution of the as-exfoliated MoS<sub>2</sub> solution with H<sub>2</sub>O.

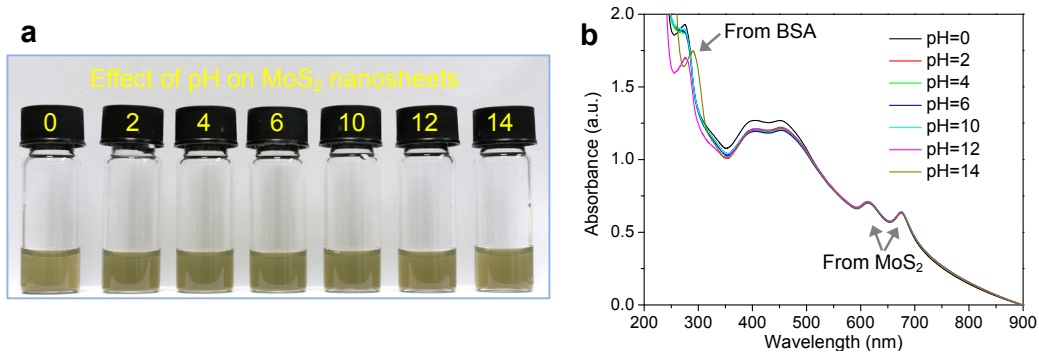


**Figure S2.** (a) Optical images and (b) UV-vis absorption spectra of BSA-adsorbed MoS<sub>2</sub> nanosheets (the as-exfoliated solution was diluted by three times) after six-day treatment under various pH values (0–14). With the change of pH, the absorption spectra of MoS<sub>2</sub> nanosheets remained unchanged while the absorption peaks of BSA clearly changed, exhibiting that the BSA-adsorbed MoS<sub>2</sub> nanosheets are very stable under different pH. This indicates that with the change of pH, the adsorption of BSA on MoS<sub>2</sub> were not affected at the interface of BSA and flat MoS<sub>2</sub> nanosheets, however, the adsorption of BSA on carbon nanotubes were easily affected at the interface of BSA and curved carbon nanotubes, which was demonstrated in earlier research to show the adsorption–desorption process of BSA on carbon nanotubes.<sup>S1,S2</sup>

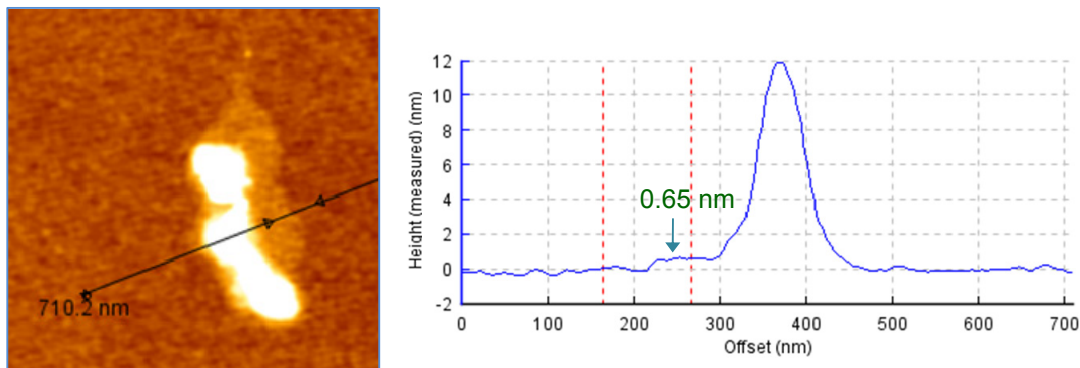


**Figure S3.** AFM image of single-layer MoS<sub>2</sub> nanosheets for demonstrating the binding of BSA on MoS<sub>2</sub> layer. The single-layer MoS<sub>2</sub> nanosheets have a thickness of 0.65 nm and the average height of BSA on MoS<sub>2</sub> is ~10 nm.

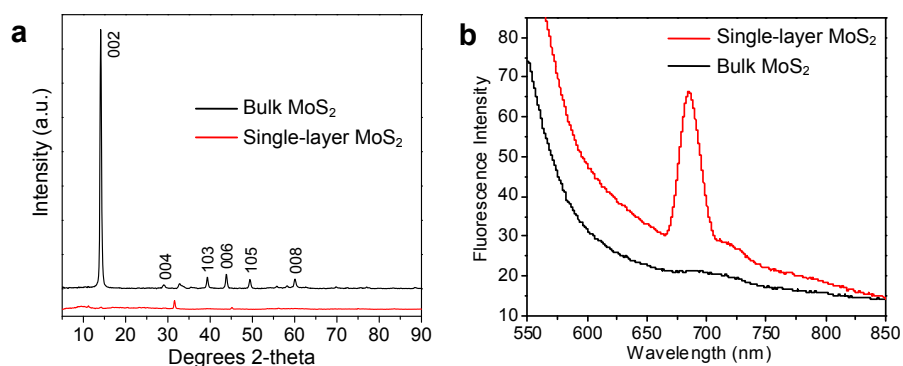


**Figure S4.** Characterization and comparison of single-layer MoS<sub>2</sub> nanosheets and bulk MoS<sub>2</sub>: (a) XRD patterns and (b) fluorescence spectra. The XRD pattern of the single-layer MoS<sub>2</sub> nanosheets did not show any of the reflection peaks from bulk MoS<sub>2</sub> (the small peak at 32° is from silicon substrate), indicating that there is no stacking of layers along *c* direction due to the formation of single-layer nanosheets. Meanwhile, a fluorescent emission at 678 nm was produced after the exfoliation of bulk MoS<sub>2</sub> to single-layer nanosheets.

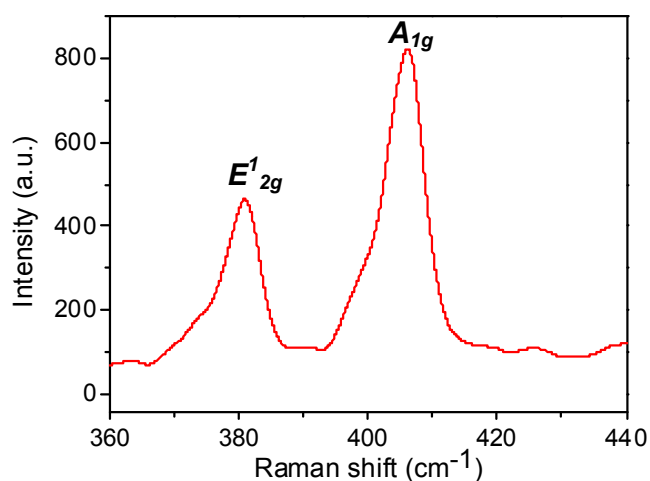


**Figure S5.** Raman spectrum of single-layer MoS<sub>2</sub> nanosheets exfoliated by sonicating MoS<sub>2</sub> powder in BSA solution. The single-layer MoS<sub>2</sub> nanosheets exhibit strong bands at 382 and 408 cm<sup>-1</sup>, which are associated with the in-plane vibration (*E'*<sub>2g</sub>) and out-of-plane vibration (*A*<sub>1g</sub>) modes, respectively. The liquid-phase exfoliated single-layer nanosheets showed the different distance between two Raman modes from the mechanically-exfoliated single-layer nanosheets,<sup>S3,S4</sup> which are not used to determine the layer number of liquid-phase exfoliated nanosheets due to surface adsorption.

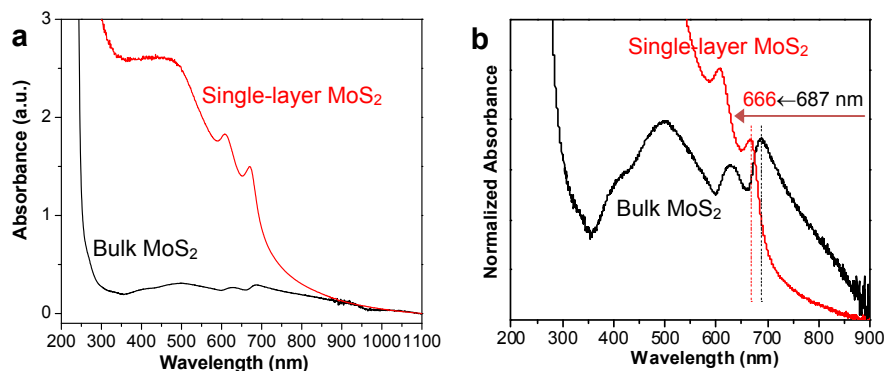


**Figure S6.** UV-vis absorption spectra of bulk MoS<sub>2</sub> and single-layer MoS<sub>2</sub> nanosheets. (a) The absorption intensity of single-layer MoS<sub>2</sub> nanosheets is five times as strong as that of bulk MoS<sub>2</sub> at ~666 nm. (b) There is a great blue-shift from 687 to 666 nm for the absorption peak after the exfoliation of bulk MoS<sub>2</sub> into single-layer MoS<sub>2</sub> nanosheets.

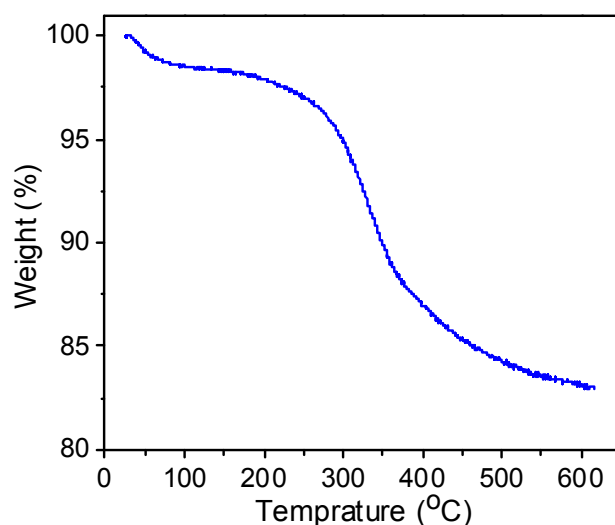


**Figure S7.** Thermogravimetric analysis (TGA) curve of single-layer MoS<sub>2</sub>-BSA nanosheets. TGA was carried out on a TGA Q5000 under the condition of 10 °C/min with a nitrogen flow at 75 mL/min. The weight loss below 100 °C is attributed to water (i.e., 98 % of sample is MoS<sub>2</sub> and BSA). In the range of 200–400 °C, the weight loss of ~17 % is mainly due to the thermal decomposition of BSA into carbon. From this value, the weight ratio of BSA and MoS<sub>2</sub> is calculated to be ~42 %, providing that the weight ratio of carbon in BSA is ~50 %. This data agrees well with the estimated value (45 %) through weighting free BSA and non-exfoliated MoS<sub>2</sub> during the preparation of single-layer MoS<sub>2</sub> (refer to the text in details).

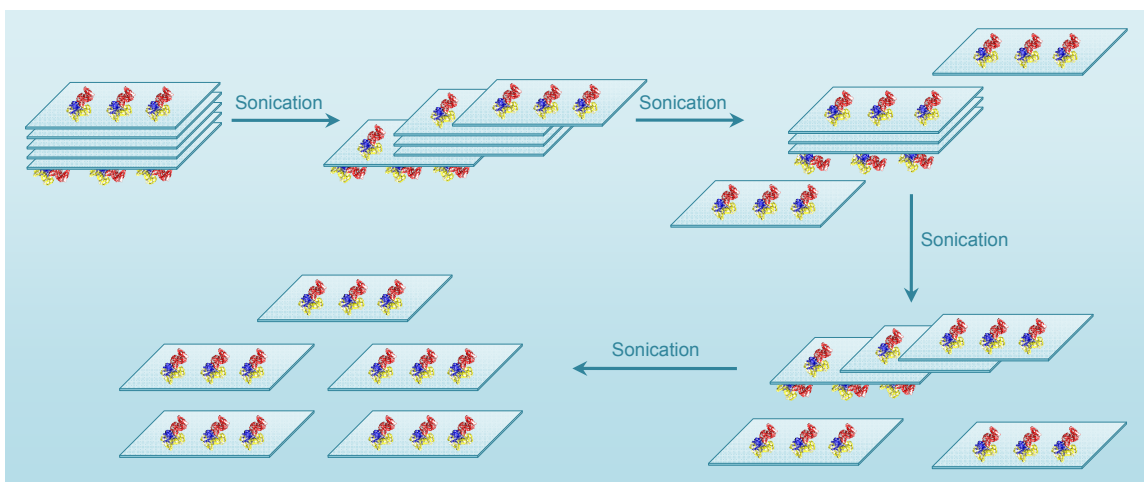


**Figure S8.** Layer-by-layer exfoliation of MoS<sub>2</sub> nanosheets in sonic bath via the strong binding of BSA on MoS<sub>2</sub> layers. After layered MoS<sub>2</sub> powder is added into BSA aqueous solution, BSA can stably bind on the surface of MoS<sub>2</sub> crystals. During sonication, the BSA-adsorbed surface layer of MoS<sub>2</sub> may slide against the layers below, and freshly exposed surfaces are then covered by BSA to prevent the reverse sliding, eventually leading to the complete exfoliation into the single-layer MoS<sub>2</sub> nanosheets. The exfoliating process proceeds repeatedly for layer-by-layer production of single-layer MoS<sub>2</sub> nanosheets in large quantity.

### Exfoliation of MoS<sub>2</sub> nanosheets with different amounts of BSA and MoS<sub>2</sub> powder

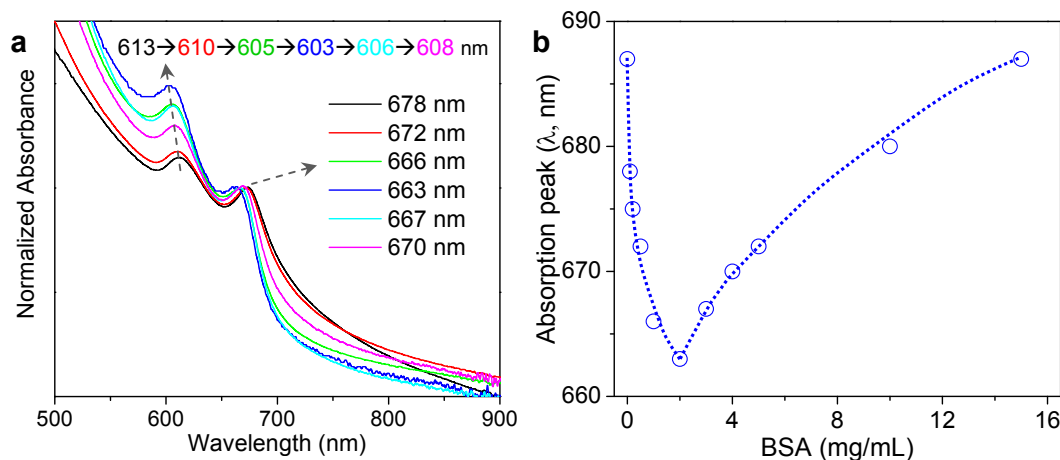


**Figure S9.** (a) UV-vis absorption spectra of various MoS<sub>2</sub> nanosheets after normalization using the intensity at ~666 nm. Their absorption peaks at ~666 nm shift from 678, 672, 666, 663, 667 to 670 nm and the absorption peaks at ~605 nm shift from 613, 610, 605, 603, 606 to 608 nm, with the increase of BSA concentrations from 0.1, 0.5, 1, 2, 3 to 4 mg/mL. (b) The absorption peaks at ~666 nm of exfoliated MoS<sub>2</sub> as a function of the used BSA concentration.

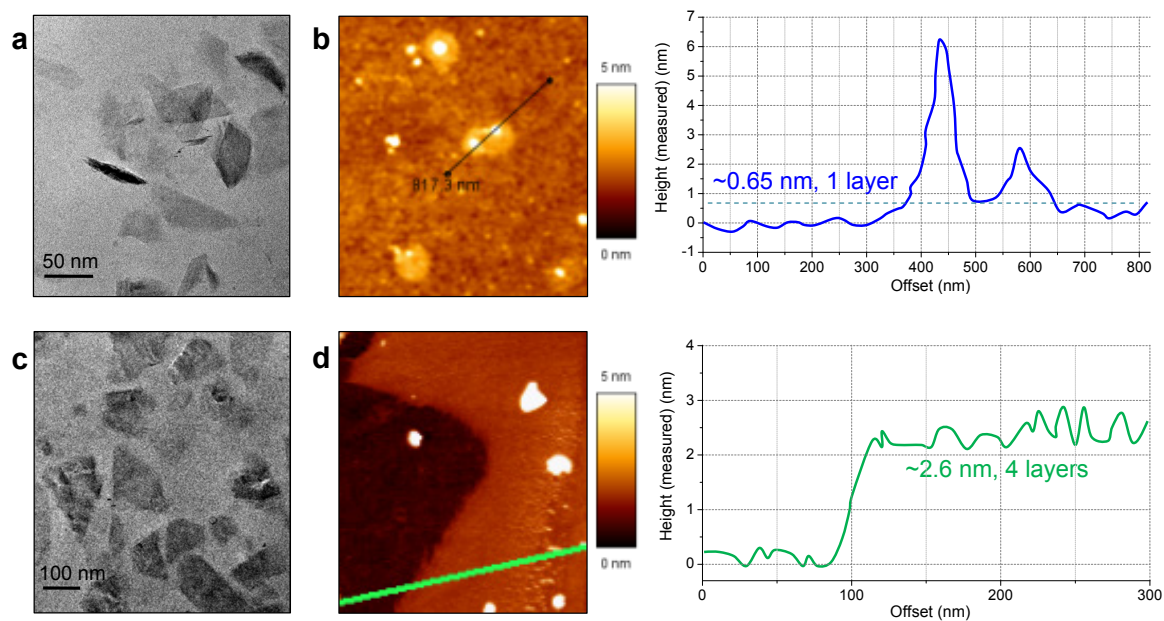


**Figure S10.** (a) TEM and (b) AFM images (with height measurement) of MoS<sub>2</sub> nanosheets exfoliated at BSA concentrations of 0.1 mg/mL. (c) TEM and (d) AFM images (with height measurement) of MoS<sub>2</sub> nanosheets exfoliated at BSA concentrations of 4 mg/mL.

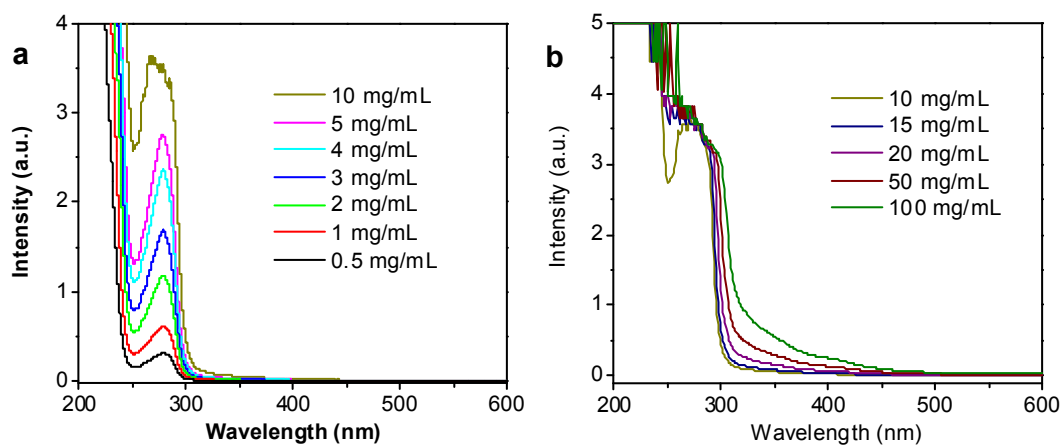


**Figure S11.** UV-vis absorption spectra of BSA solution with an increase of BSA concentrations. (a) 0.5–10 mg/mL and (b) 10–100 mg/mL.

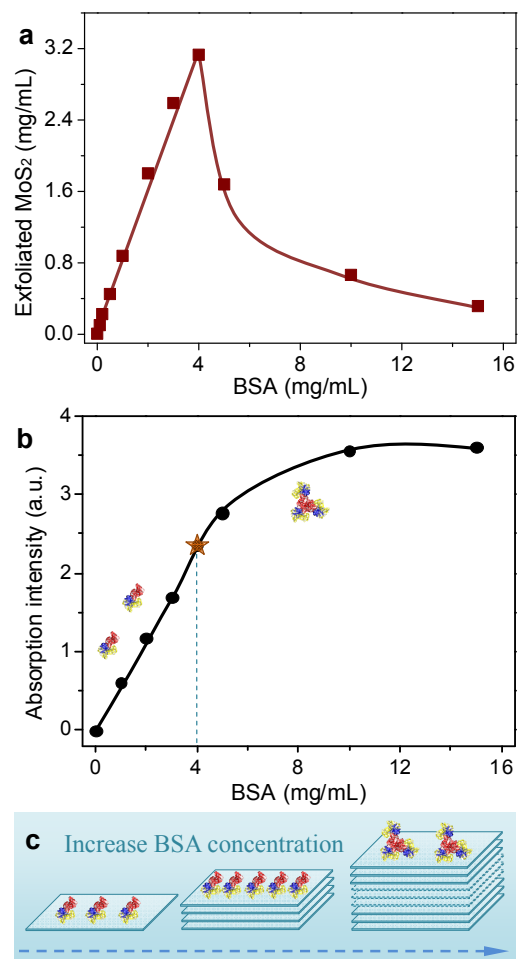


**Figure S12.** Effect of BSA concentration on the exfoliation of MoS<sub>2</sub> nanosheets. (a) BSA concentration-dependent exfoliation of MoS<sub>2</sub> nanosheets. (b) The evolution of absorption intensity of BSA at 278 nm in BSA solution with the increase of BSA concentration. (c) Schematic for the exfoliation of MoS<sub>2</sub> nanosheets with increase of BSA concentration.

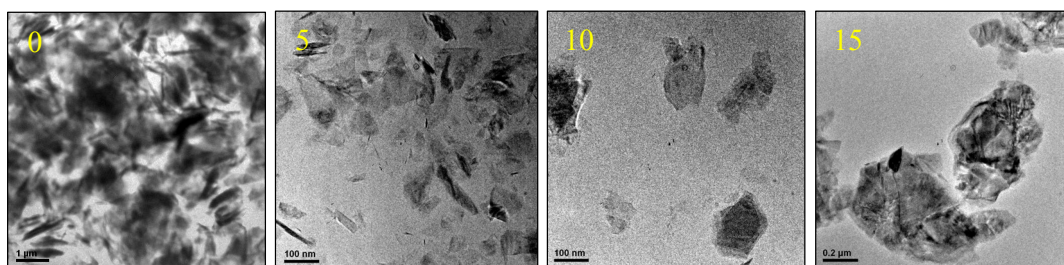


**Figure S13.** TEM observations of MoS<sub>2</sub> products obtained at BSA concentrations of 0, 5, 10 and 15 mg/mL.

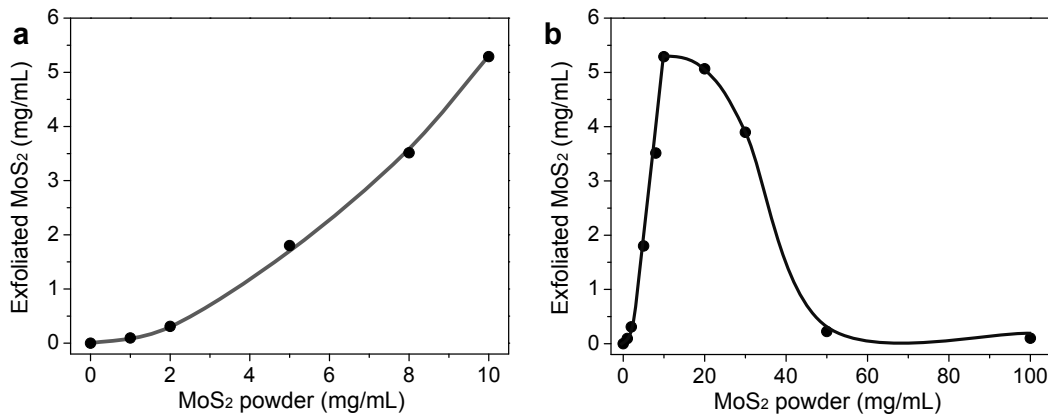


**Figure S14.** MoS<sub>2</sub> amount-dependent exfoliation of MoS<sub>2</sub> nanosheets at a fixed BSA concentration of 1 mg/mL: (a) 0–10 mg/mL and (b) 0–100 mg/mL.

The single-layer MoS<sub>2</sub> nanosheets were obtained by exfoliating MoS<sub>2</sub> powder with the use of 5 mg/mL MoS<sub>2</sub> and 1 mg/mL BSA. The influence of BSA concentrations was further studied on the controlled production of MoS<sub>2</sub> nanosheets. Experimentally, MoS<sub>2</sub> nanosheets were obtained at high yield after sonication for 48 h at the concentration of BSA ranging 0.1, 0.5, 1, 2, 3 to 4 mg/mL. Their well dispersion and high stability allow us to investigate the evolution of absorption wavelength of MoS<sub>2</sub> nanosheets with the change of BSA concentrations (Figure S9a). With the increase of BSA concentrations from 0.1, 0.5, 1 to 2 mg/mL, single-layer MoS<sub>2</sub> nanosheets were produced (Figure S10a and b) while there was a blue-shift of their absorption peaks from 678, 672, 666 to 663 nm, respectively. This is because the sheet sizes were decreased with the increase of BSA concentration, which led to the more non-uniform adsorption of BSA to cause fracture of MoS<sub>2</sub> layer. With the further increase of BSA concentrations from 2 to 3 and 4 mg/mL, a red-shift of their absorption peaks from 663, to 667 and 670 nm was observed (Figure S9a), indicating the formation of multilayer nanosheets (Figure S10c and d). With the continuous increase of BSA concentrations to 5, 10 and 15 mg/mL, a more red-shift of their absorption peaks from 672, to 680 and 687 nm was observed (Figure S9b), indicating the exfoliation efficiency for MoS<sub>2</sub> nanosheets was decreased to nearly zero.

As shown in Figure S12a, with the increase of BSA concentration (0.1 to 15 mg/mL) at a fixed MoS<sub>2</sub> at 5 mg/mL, the amount of exfoliated MoS<sub>2</sub> nanosheets first increased quickly and then decreased slowly. One observed a linear relationship between the exfoliated amounts of MoS<sub>2</sub> and the used amounts of BSA up to 4 mg/mL. Beyond 4 mg/mL, the exfoliated amount of MoS<sub>2</sub> decreased non-linearly with the further increase of BSA concentration. Interestingly, in pure BSA solution, the absorption intensity also increased linearly with the increase of BSA concentration below 4 mg/mL and its absorption then increased slowly with the further increase of BSA concentration (Figure S11 and S12b), indicating the formation of BSA aggregates at higher concentration. Overall, lower concentration of BSA in the form of monomers can strongly adsorb on bulk MoS<sub>2</sub>, leading to the effective formation of MoS<sub>2</sub> nanosheets under sonication (Figure S12c). In comparison, higher concentration of BSA in the form of aggregates<sup>S5</sup> cannot strongly adsorb on bulk MoS<sub>2</sub>, leading to the ineffective formation of MoS<sub>2</sub> nanosheets, as confirmed by TEM observations (Figure S13). This is because the BSA aggregates are formed via hydrophobic interaction between BSA monomers,<sup>S5</sup> and thus they become difficult to adsorb on MoS<sub>2</sub> by the hydrophobic segments of BSA. Furthermore, at a fixed BSA of 1 mg/mL, the exfoliated amount of MoS<sub>2</sub> nanosheets increased quickly and quasi-linearly with the increase of MoS<sub>2</sub> amount up to 10 mg/mL, and then decreased gradually with the further increase of MoS<sub>2</sub> amount up to 100 mg/mL (Figure S14). These results show that the exfoliation process is highly dependent on the ratio of BSA/MoS<sub>2</sub> used.

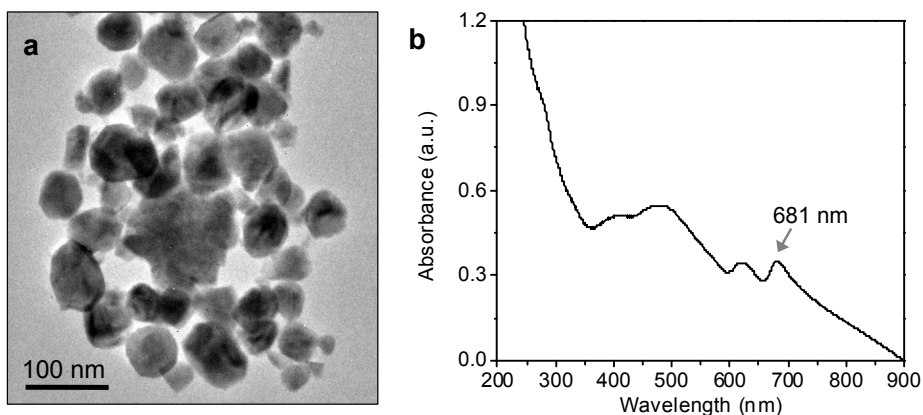


**Figure S15.** (a) TEM image and (b) UV-vis absorption spectrum of MoS<sub>2</sub> product by using a sonic tip with a power of 60 W. Experimentally, 50 mg of MoS<sub>2</sub> powder and 10 mg of BSA were added into 10 mL of aqueous solution. The mixed suspension was sonicated by using a sonic tip for 1 h, and the resulting solution was then centrifuged at 1500 rpm for 20 min to obtain the supernatant with MoS<sub>2</sub> product. One can see that MoS<sub>2</sub> powder was easily broken into particles with an average size of ~80 nm under the sonic tip rather than nanosheets. This indicates that the sonic tip cannot be used for layer-by-layer exfoliation of MoS<sub>2</sub> nanosheets.

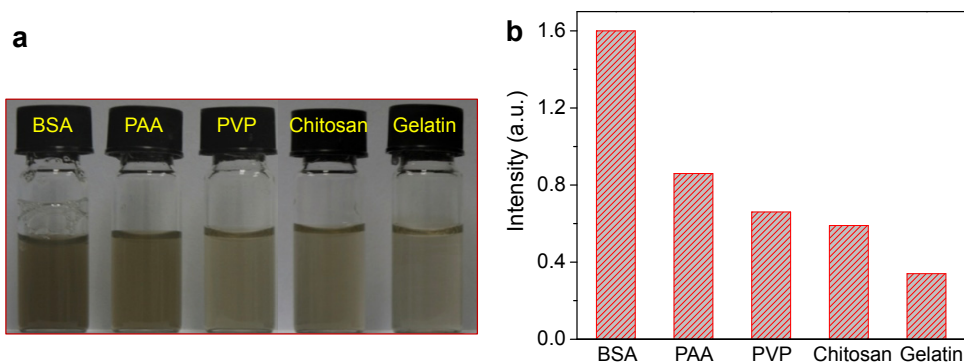


**Figure S16.** Exfoliation of MoS<sub>2</sub> nanosheets by the use of various polymers. (a) Optical images of MoS<sub>2</sub> nanosheets exfoliated in the presence of different polymers (after diluted the as-exfoliated solutions for four times). (b) Absorption intensity of the as-exfoliated MoS<sub>2</sub> nanosheets in the presence of different polymers.

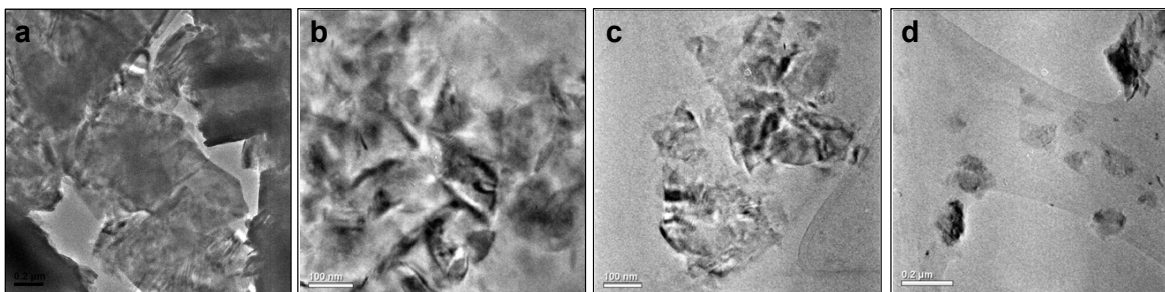


**Figure S17.** TEM images of MoS<sub>2</sub> nanosheets exfoliated in the presence of different polymers: (a) PAA, (b) PVP, (c) chitosan and (d) gelatin. It is seen that these polymers are not able to successfully exfoliate single-layer MoS<sub>2</sub> nanosheets in water.

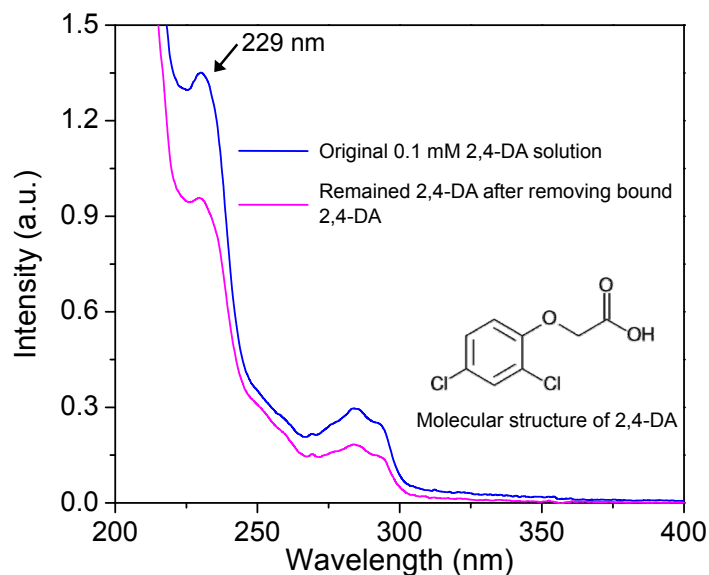


**Figure S18.** The bound amount of 2,4-DA by MoS<sub>2</sub>-BSA nanosheets. Experimentally, 5 mg MoS<sub>2</sub>-BSA nanosheets were dispersed into 5 mL of 0.1 mM 2,4-DA solution (methanol:H<sub>2</sub>O=4:1, v/v). After the mixture solution was incubated on a rocking table with shaking at 300 rpm for 12 h, the MoS<sub>2</sub> nanosheets were discarded from the solution phase by centrifugation at 10000 rpm for 10 min. UV-vis absorption spectra of the original 2,4-DA solution (0.1 mM) and the remained solution after removal of MoS<sub>2</sub> were measured, as blue and pink line. The bound amount of 2,4-DA was calculated as 150 nmol according to the equation:  $Q=(I_0-I)VC/I_0$ , where  $V$  is the volume of solution and  $C$  is the concentration of 2,4-DA;  $I_0$  and  $I$  are the original and remained absorption intensity at 229 nm, respectively.

## Specific capacitance of various MoS<sub>2</sub> nanosheets from cyclic voltammetry

To quantitatively evaluate the charge storage capacity, the specific capacitance of the composites is determined by the expression: *voltammetric charge / (potential window × composite loading)*. Considering that the anodic voltammetric charges and cathodic voltammetric charges are not same because the shape of CV curves is not in the ideal mirror-symmetry, we use integral area of CV curve/scan rate to represent the sum of anodic and cathodic voltammetric charges, i.e., voltammetric charge. So the specific capacitance is calculated on the basis of the following equation:  $C = \int_{E_1}^{E_2} i(E)dE / 2(E_2-E_1)mv$ , where  $C$  is the specific capacitance of individual sample,  $E_1$  and  $E_2$  are the cutoff potentials in cyclic voltammetry,  $i(E)$  is the instantaneous current,  $\int_{E_1}^{E_2} i(E)dE$  is the total voltammetric charge obtained by integration of positive and negative sweep in cyclic voltammograms,  $(E_2-E_1)$  is the potential window width,  $m$  is the mass of individual sample, and  $v$  is the potential scan rate.

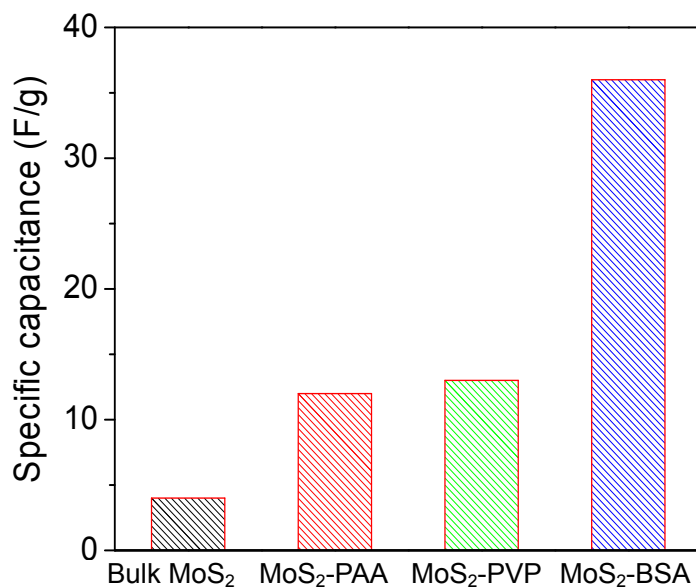


**Figure S19.** Specific capacitance of various MoS<sub>2</sub> materials at scan rate of 100 mV/s. It is seen that MoS<sub>2</sub>-BSA nanosheets have the highest specific capacitance.

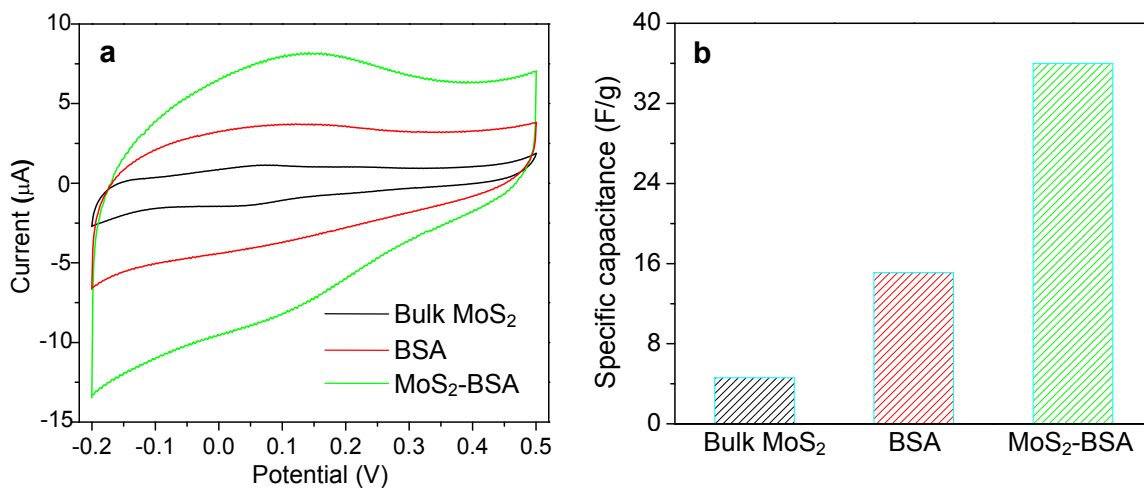


**Figure S20.** Comparison on the specific capacitance of different materials. (a) Cyclic voltammetric curves of bulk  $\text{MoS}_2$ , BSA and  $\text{MoS}_2$ -BSA nanosheets at scan rate of 100 mV/s. (b) Comparison on specific capacitance of different materials at the same amount.

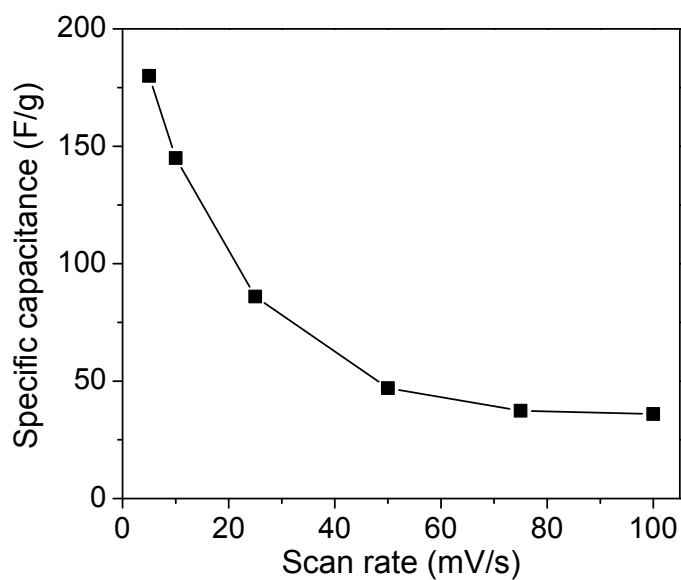


**Figure S21.** The evolution of specific capacitance of  $\text{MoS}_2$ -BSA nanosheets with scan rate.

**Table S1.** Amino acid sequences of BSA. Each BSA molecule contains 583 amino acids. Among them, there are 27 phenylalanine (F, highlighted in red) and 35 cysteine (C, highlighted in blue) to form 17 disulfide bonds while remaining one free thiol group.

1	DTHKSEIAHR	FKDLGEEHFK	GLVLIAFSQY	LQQCPFDEHV
2	KLVELTEFA	KTCVADESHA	GCEKSLHTLF	GDELCKVASL
3	RETYGDMADC	CEKQEPERNE	CFLSHKDDSP	DLPKLPDPN
4	TLCDEFKADE	KKFWGKYLYE	IARRHPYFYA	PELLYYANKY
5	NGVFQECQA	EDKGA CLLPK	IETMREKVL T	SSARQRLRCA
6	SIQKFGERAL	KAWSVARLSQ	KFPKAEFVEV	TKLVTDLTKV
7	HKECCHGDDL	ECADDRADLA	KYICDNQDTI	SSKLKECCDK
8	PLLEKSHCIA	EVEKDAIPED	LPPLTADFAE	DKDVCKNYQE
9	AKDAFLGSFL	YEYSRRHPEY	AVSVLLRLAK	EYEATLEEC
10	AKDDPHACYT	SVFDKCLKHLV	DEPQNLIKQN	CDQFEKLG EY
11	GFQNALIVRY	TRKVPQVSTP	TLVEVSRSLG	KVGTRCCTKP
12	ESERMPCTED	YLSLILNRLC	VLHEKTPVSE	KVTKCCTESL
13	VNRRPCFSAL	TPDETYVPKA	FDEKLFTHA	DICTLPDTEK
14	QIKKQTALVE	LLKHKPKATE	EQLKTMENF	VAFVDKCCAA
15	DDKEACFAVE	GPKLVVSTQT	ALA	

**Table S2.** The first-principles simulation of the binding energies of different functional groups at the edge of MoS<sub>2</sub> nanosheet. Similar with those on the basal plane, the benzene rings and disulfides have higher binding energies than other polar groups. In comparison, the binding energies of the functional groups at the edge are larger than those on the basal plane. This is due to the presence of dangling bonds and edge states located at the edges of MoS<sub>2</sub> nanosheets.<sup>S6</sup> That is to say, the functional groups of BSA have stronger interactions at the edge of nanosheets than those on the basal plane of nanosheets. However, as a whole rather than individual groups, BSA has weaker interaction at the edge than those on the basal plane because there is a much smaller contact area of BSA at the edge of nanosheets than that on the basal plane. As a consequence, BSA can stably bind on the basal plane as compared to that at the edge of nanosheets, which was demonstrated by AFM observation (Figure 1c).

Special group of BSA	-OH	-SH	-NH <sub>2</sub>	-COOH	-SS-	-C <sub>6</sub> H <sub>5</sub>
Binding energies on MoS <sub>2</sub> edge (eV)	0.88	0.99	1.03	0.93	1.10	1.08

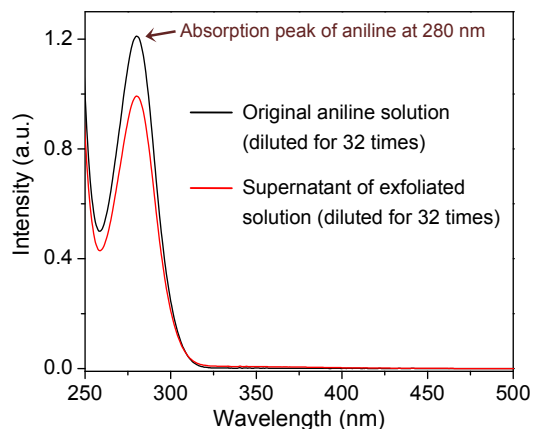


**Figure S22.** Surface binding of aniline on MoS<sub>2</sub> powder. After adding 50 mg of MoS<sub>2</sub> powder into 10 mL of aqueous solution containing 10 mg of aniline and sonicating for 48 h, MoS<sub>2</sub> product was precipitated within 0.5 h. By comparing the absorption intensities of the clear supernatant (red line) and original aniline solution (black line), the bound amount of aniline on MoS<sub>2</sub> powder was calculated to be 1.8 mg.

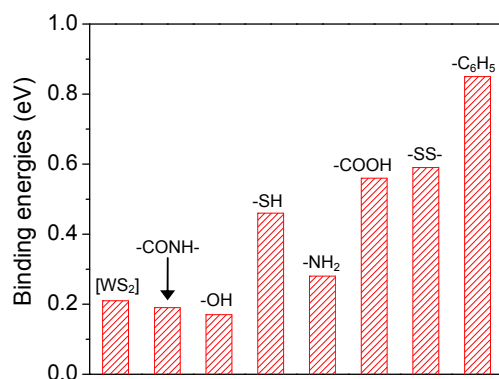


**Figure S23.** The binding energies of various specific groups on WS<sub>2</sub> layer, which were calculated by the first-principles calculation software VASP with the non-local van der Waals optB88 functional. [WS<sub>2</sub>] is the binding energy between two adjacent WS<sub>2</sub> layers.

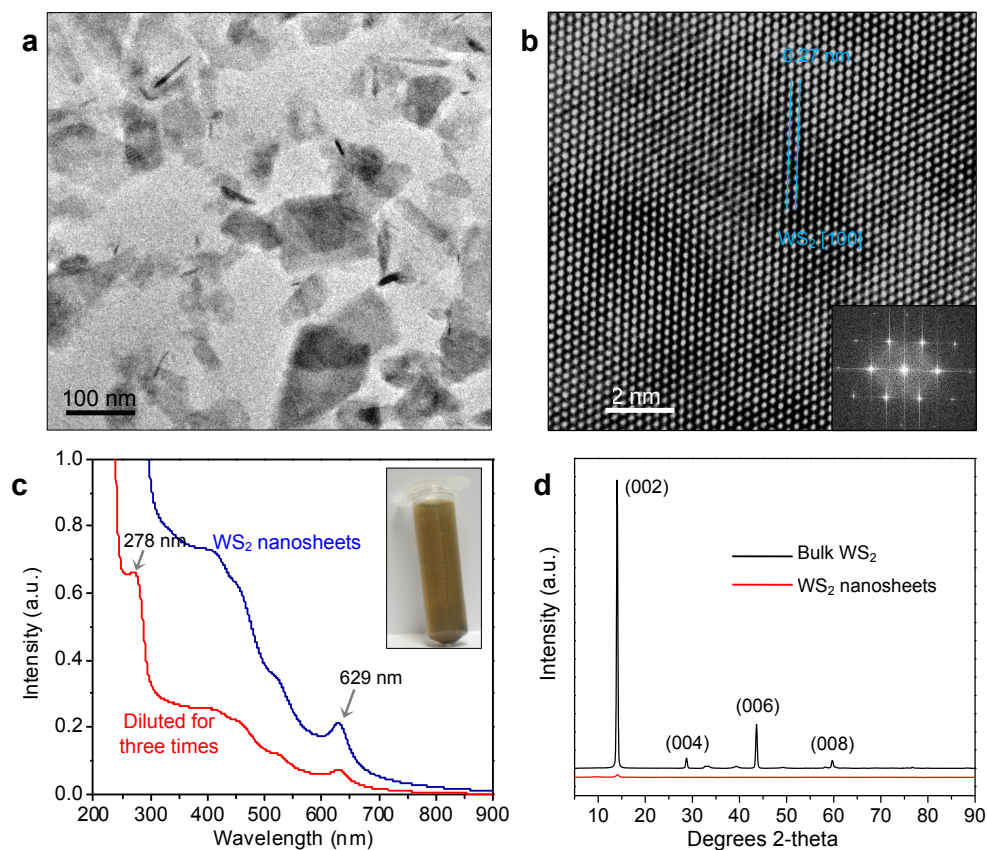


**Figure S24.** Characterization of WS<sub>2</sub> nanosheets exfoliated via sonicating the mixture of 50 mg WS<sub>2</sub> and 10 mg BSA in 10 mL of H<sub>2</sub>O for 48 h. (a) Low-resolution and (b) high-resolution TEM image of WS<sub>2</sub> nanosheet. Inset in (b) is the fast Fourier transform pattern and the spacing fringe of 0.27 nm is from the reflection of WS<sub>2</sub> (100) facets. (c) UV-vis absorption spectrum of WS<sub>2</sub> nanosheets (inset is the optical image of WS<sub>2</sub> solution). The absorption peak at 629 nm from WS<sub>2</sub> nanosheets is attributed to the direct excitonic transitions at the K point of Brillouin zone.<sup>S7</sup> After diluting by three times, the absorption peak of BSA (278 nm) was observed to indicate the binding of BSA on WS<sub>2</sub> nanosheets. (d) XRD patterns of WS<sub>2</sub> nanosheets and bulk MoS<sub>2</sub>.

**Table S3.** The binding energies of different functional groups on WSe<sub>2</sub> layer. These binding energies were calculated by the software VASP with the non-local van der Waals optB88 functional.

Special group of BSA	-OH	-SH	-NH <sub>2</sub>	-COOH	-SS-	-C <sub>6</sub> H <sub>5</sub>
Binding energies on WSe <sub>2</sub> layer (eV)	2.28	5.12	2.03	5.76	5.54	9.16

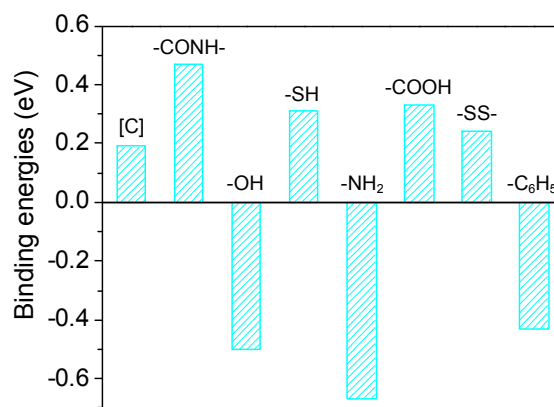


**Figure S25.** The binding energies of various specific groups on graphene. [C] is the binding energy between two adjacent graphenes. Note that the positive value means a stable adsorption, whereas the negative value means an unstable adsorption. The DFT simulation indicates that the peptide bonds rather than benzene rings play a major role in exfoliating graphene. The peptide bonds can strongly bind graphene with positive binding energy for their exfoliation whereas the benzene rings are not adsorbed on graphene with negative binding energy, indicating that fibroin without benzene rings is more effective to bind on graphene than BSA with benzene rings. Therefore, fibroin is more effective for exfoliation of graphene as compared to BSA. Experimentally, the resulting concentration of graphene when using BSA is 0.85 mg/mL, while the concentration of graphene when using fibroin is obtained as high as 1.66 mg/mL.

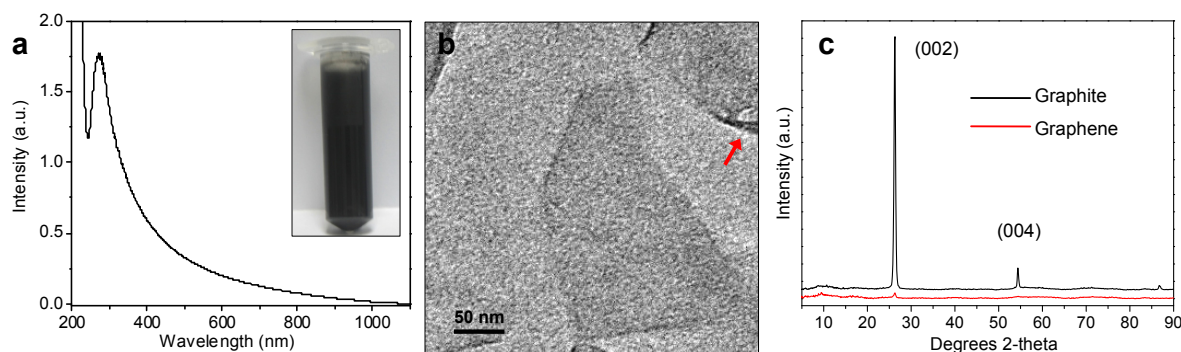


**Figure S26.** Characterization of graphene exfoliated via sonicating the mixture of 50 mg graphite and 5 mg BSA in 10 mL of H<sub>2</sub>O for 48 h. (a) UV-vis absorption spectrum, (b) TEM image and (c) XRD pattern of graphene. The as-obtained solution was diluted for 10 times to collect its absorption spectrum. Inset in (a) is the optical image of the as-obtained graphene. By comparing with MoS<sub>2</sub> nanosheets, it is interesting to observe the curled graphene in TEM image (highlighted by red arrow), indicating the much higher rigidity of MoS<sub>2</sub> nanosheets than graphene. The elastic bending modulus of single-layer MoS<sub>2</sub> is obtained as 9.61 eV based on the developed Stillinger–Weber potential,<sup>S8,S9</sup> whereas the bending modulus of graphene is only 1.4 eV. The elastic bending modulus for MoS<sub>2</sub> nanosheets is larger than that of graphene by a factor of ~7. It was found that the finite thickness of single-layer MoS<sub>2</sub> (1 Mo monolayer and 2 S monolayers) play a major role in this substantial enhancement in bending modulus as compared to graphene.<sup>S9</sup>

### Complete Citation for Reference 9a:

Coleman, J. N.; Lotya, M.; O'Neill, A.; Bergin, S. D.; King, P. J.; Khan, U.; Young, K.; Gaucher, A.; De, S.; Smith, R. J.; Shvets, I. V.; Arora, S. K.; Stanton, G.; Kim, H.-Y.; Lee, K.; Kim, G. T.; Duesberg, G. S.; Hallam, T.; Boland, J. J.; Wang, J. J.; Donegan, J. F.; Grunlan, J. C.; Moriarty, G.; Shmeliov, A.; Nicholls, R. J.; Perkins, J. M.; Grievson, E. M.; Theuwissen, K.; McComb, D. W.; Nellist, P. D.; Nicolosi, V. *Science* **2011**, *331*, 568.

### References Cited in the Supporting Information:

- (S1) Edri, E.; Regev, O. *Anal. Chem.* **2008**, *80*, 4049.
- (S2) Valenti, L. E.; Fiorito, P. A.; García, C. D.; Giacomelli, C. E. *J. Colloid Interface Sci.* **2007**, *307*, 349.
- (S3) Wu, W.; Wang, L.; Li, Y.; Zhang, F.; Lin, L.; Niu, S.; Chenet, D.; Zhang, X.; Hao, Y.; Heinz, T. F.; Hone, J.; Wang, Z. L. *Nature* **2014**, *514*, 470.
- (S4) Zeng, Z.; Yin, Z.; Huang, X.; Li, H.; He, Q.; Lu, G.; Boey, F.; Zhang, H. *Angew. Chem. Int. Ed.* **2011**, *50*, 11093.
- (S5) Lee, S. J.; Scotti, N.; Ravasio, N.; Chung, I. S.; Song, H. *Cryst. Growth Des.* **2013**, *13*, 4131.
- (S6) Cai, Y.; Zhang, G.; Zhang, Y. W. *J. Am. Chem. Soc.* **2014**, *136*, 6269.
- (S7) Li, C.; Wang, T.; Wu, Y.; Ma, F.; Zhao, G.; Hao, X. *Nanotechnology* **2014**, *25*, 495302.
- (S8) Jiang, J.-W.; Qi, Z.; Park, H. S.; Rabczuk, T. *Nanotechnology* **2013**, *24*, 435705.
- (S9) Castellanos-Gomez, A.; van Leeuwen, R.; Buscema, M.; van der Zant, H. S. J.; Steele, G. A.; Venstra, W. J. *Adv. Mater.* **2013**, *25*, 6719.